Green Chemistry

PAPER

View Article Online
View Journal | View Issue

Cite this: *Green Chem.*, 2026, **28**, 7827

Electrochemical nitrate-to-ammonia conversion over a broad concentration range *via* a hollow Co_3O_4/CuO catalyst

Li Yao,[a,b] Shao Ye,[a] Zhe Li,[c] Mingjie Tuo,[b] Yibin Cui,[c] Zhenbin Wang,[a] Zhenhua Xie,[d] Wenlei Zhu *[b] and Bo Shen *[a]

Received 23rd January 2026,
Accepted 9th April 2026

DOI: 10.1039/d6gc00484a

rsc.li/greenchem

Widespread nitrate contamination in water challenges both aquatic ecosystems and drinking water safety, and the electrocatalytic nitrate reduction to ammonia (eNRA) presents a promising sustainable way to convert pollutants to value-added products. However, most existing eNRA systems operate efficiently only under highly alkaline and concentrated conditions that are incompatible with real wastewater. Herein, we report a hollow heterostructured Co_3O_4/CuO catalyst that permits efficient eNRA in neutral aqueous media over a wide range of environmentally relevant nitrate concentrations (1–250 mM). The catalyst achieves NH_3 faradaic efficiencies above 97% in the 10–250 mM nitrate range and maintains a faradaic efficiency of 86% even at 1 mM nitrate. Furthermore, the catalyst exhibited excellent stability over 100 hours of continuous operation. *In situ* Fourier transform infrared spectroscopy analysis suggests that the hollow architecture creates a spatially confined microenvironment that accelerates the hydrogenation of NO_x intermediates toward NH_3, and density functional theory calculations indicate the ensemble effect of Co_3O_4 and CuO in reducing the free-energy changes of key nitrate reduction steps. This work highlights a structural engineering strategy in electrocatalysts for efficient nitrate remediation and wastewater treatment.

Green foundation

1. This work demonstrates a sustainable electrochemical route for converting nitrate into ammonia using Earth-abundant catalysts, enabling pollutant-to-value conversion while avoiding the chemical input and secondary waste associated with conventional biological and physicochemical treatments.
2. The system achieves up to 97% faradaic efficiency for NH_3 production over a wide nitrate concentration range (10–250 mM) and maintains 86% faradaic efficiency at environmentally relevant low concentration (1 mM) under neutral conditions, thereby reducing reliance on strongly alkaline electrolytes and minimizing the need for downstream neutralization.
3. Further work will focus on coupling with renewable electricity and evaluating performance in complex wastewater to further assess practical environmental benefits, and exploring the simultaneous conversion of co-existing pollutants to enhance overall environmental impact.

Introduction

Nitrate accumulation in aquatic environments has become increasingly widespread.[1–4] In environmental monitoring, nitrate concentrations above 50 mg L^{-1} (~0.8 mM) are commonly considered beyond drinking-water standards set by the World Health Organization.[5] Conventional nitrate remediation strategies, such as biological denitrification and physicochemical separation, mainly focus on nitrate removal through reduction to N_2 or physical separation from water. While effective at controlling nitrate contamination, these approaches involve substantial energy consumption and provide limited capability for resource recovery.[6–10] For example, biological denitrification generates substantial CO_2 emissions due to the oxidation of organic carbon sources, accompanied by additional N_2O emissions and excess sludge production that require secondary treatment.[11] In parallel, physicochemical separation methods, such as ion exchange and reverse osmosis, require chemical inputs for resin

[a]*Department of Materials Science and Engineering, City University of Hong Kong, Hong Kong, China*
[b]*School of Environment, Nanjing University, Nanjing, China*
[c]*Nanjing Institute of Environmental Sciences, Ministry of Ecology and Environment, Nanjing, China*
[d]*Department of Chemistry, University of Science and Technology of China, Hefei, China*

regeneration or membrane cleaning, and generate concentrated brine streams that create additional disposal challenges.[12–15] In contrast, electrocatalytic nitrate reduction to ammonia (eNRA) has recently emerged as a promising strategy that simultaneously removes nitrate while producing ammonia, which serves as a fundamental chemical feedstock.[16–19] When driven by renewable electricity, eNRA provides a sustainable opportunity to couple water purification with green chemical synthesis.[20–23] Compared with conventional treatment methods, eNRA can potentially reduce the environmental footprint of nitrate remediation. For example, recent studies have demonstrated that electrochemical denitrification systems can reduce CO_2 emissions by up to 79.5% compared to biological denitrification, with energy consumption as low as 9.97 kWh kg^{-1} N under optimized conditions.[17,24] Moreover, theoretical analyses indicate that the minimum energy requirement for nitrate-to-ammonia conversion is approximately 6.5 kWh kg^{-1} NH_3, which is lower than that of the Haber–Bosch method (10–13 kWh kg^{-1}) from N_2,[25,26] suggesting its potential as a low-energy pathway for ammonia production. However, most existing eNRA systems are operated under highly alkaline and concentrated nitrate conditions (*e.g.*, pH ≥ 13, nitrate concentration ≥ 0.1 M) that are very different from those in real wastewater matrices.[27–31] First, nitrate concentrations can span a wide range and fluctuate over orders of magnitude from agricultural to industrial wastewater, while many catalysts used in eNRA are often optimized for a narrow concentration regime. At low nitrate concentrations, eNRA can lead to accumulation of nitrite intermediates, which lowers ammonia selectivity and introduces additional toxicity concerns.[32,33] Second, the pH of most municipal wastewater is close to neutral (typically pH 6–8).[34,35] Maintaining strongly alkaline electrolytes requires the continuous addition of base (*e.g.*, KOH or NaOH). As a result, subsequent pH neutralization prior to discharge or reuse is needed to convert these chemicals into dissolved salts (*e.g.*, K_2SO_4 or NaCl), which increases chemical consumption and generates salt-containing secondary waste streams. To address these challenges, an ideal eNRA catalyst should satisfy several key requirements: maintaining high selectivity across a wide nitrate concentration range, rapidly consuming reaction intermediates to avoid toxic by-products, and remaining structurally stable during long-term operation under neutral electrolyte conditions.[36–40] However, despite recent progress, achieving all these requirements within a single catalytic system remains difficult.[41–43]

Herein, we report a hollow heterostructured Co_3O_4/CuO catalyst that meets these requirements (Fig. 1). The hollow architecture creates a confined reaction environment for nitrate species within the catalyst interior, which mitigates performance loss under dilute conditions. Meanwhile, atomic ensemble effects at the Co_3O_4/CuO interface facilitate nitrate reduction and subsequent hydrogenation, promoting rapid consumption of reactive nitrogen intermediates. As a result, the catalyst maintains high NH_3 selectivity over a wide nitrate concentration range above commonly accepted pollution thresholds, spanning 1–250 mM in neutral electrolyte, with stable performance over 100 h of continuous operation.

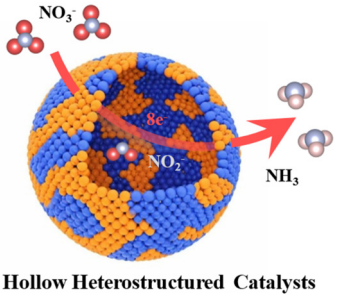

Fig. 1 Schematic diagram of hollow heterostructured Co_3O_4/CuO catalysts for eNRA (yellow and blue colours denote Co_3O_4 and CuO nanosized domains, respectively).

Experimental

Chemicals

All the reagents used were of analytical grade without further purification. Cobalt(II) nitrate hexahydrate ($Co(NO_3)_2{\cdot}6H_2O$, 99%), glycerol ($C_3H_8O_3$, 99%), isopropanol (C_3H_8O, ≥99.5%), anhydrous ethanol (C_2H_6O), sulfanilamide ($C_6H_8N_2O_2S$, 99%), ethylene glycol ($C_2H_6O_2$, ≥99.5%) and hydrochloric acid (HCl, AR) were purchased from Macklin. Copper(II) nitrate hemipentahydrate ($Cu(NO_3)_2{\cdot}2.5H_2O$, 98%) and potassium sulfate (K_2SO_4, 99%) were obtained from Jiuding Chemical. Copper foam was supplied by Suzhou Keshenghe Metal Materials. Sodium citrate ($C_6H_5Na_3O_7$, 99%), salicylic acid ($C_7H_6O_3$, 99%), sodium hydroxide (NaOH, 98%), sodium hypochlorite (NaClO, 4%), naphthyldiethylenediamine hydrochloride ($C_{12}H_{14}N_2{\cdot}2HCl$, 99%), nitric acid ($HNO_3$, 65.0–68.0%), sodium nitroferricyanide dihydrate ($Na_2[Fe(CN)_5NO]{\cdot}2H_2O$, 99%), dimethyl sulfoxide (DMSO, 99%), phosphoric acid (H_3PO_4, ≥85.0%), deuteroxide (D_2O) and potassium nitrate (KNO_3, 99%) were bought from Aladdin Biochemical Technology. Potassium nitrate-^{15}N ($K^{15}NO_3$, 99 atom% ^{15}N) was purchased from Meryer Biochemical Technology Co., Ltd (Shanghai, China). Aqueous solutions were prepared with Millipore water (18.2 MΩ cm^{-1}).

Material synthesis

Hollow Co_3O_4/CuO nanoparticles were synthesized by a hydrothermal method followed by annealing. Typically, 0.4 mmol $Co(NO_3)_2{\cdot}6H_2O$ and 0.2 mmol $Cu(NO_3)_2{\cdot}2.5H_2O$ were dissolved in a mixed solvent of 16 mL $C_3H_8O_3$ and 60 mL C_3H_8O under continuous stirring. The solution was then transferred to a 100 mL Teflon-lined stainless-steel autoclave and heated at 180 °C for 6 h. After cooling to room temperature, the Co/Cu-glycerate was collected by centrifugation, washed thoroughly with anhydrous ethanol, and freeze-dried. Finally,

the precursor was annealed in air at 400 °C for 2 h with a ramp rate of 5 °C min^{-1} to obtain the hollow Co_3O_4/CuO nanoparticles. Co_3O_4/CuO nanoparticles with different Co/Cu molar ratios (total metal amount fixed at 0.6 mmol) and single-component CuO were synthesized under the same conditions. For the synthesis of solid Co_3O_4/CuO nanoparticles, 4 mmol $Cu(NO_3)_2{\cdot}2.5H_2O$ and 4 mmol $Co(NO_3)_2{\cdot}6H_2O$ were co-precipitated in aqueous solution using NaOH. After washing several times until pH = 7, the suspension was transferred to a 100 mL PTFE-lined stainless-steel autoclave, where a hydrothermal reaction was performed at 200 °C for 12 h. The resulting precipitate was washed, collected, and annealed in air at 400 °C for 2 h, resulting in the formation of solid CoCu nanoparticles. Cu foam-supported Co_3O_4/CuO was synthesized using the same procedure, except pre-cleaned copper foam was immersed in the precursor solution prior to the reaction.

Characterization and electrochemical measurements

Scanning electron microscopy (SEM) images were acquired using a JSM-7800F microscope. X-ray diffraction (XRD) patterns were recorded on a Shimadzu XRD-6000 diffractometer. Transmission electron microscopy (TEM), high-resolution TEM (HRTEM), and energy-dispersive X-ray spectroscopy (EDS) analyses were performed using a JEM-2800 microscope. X-ray photoelectron spectroscopy (XPS) measurements were conducted using a PHI 5000 VersaProbe system. UV-visible absorption spectra were recorded using a Shimadzu UV-3600 spectrophotometer and an Agilent BioTek Synergy H1 microplate reader. Fourier transform infrared (FTIR) spectra were acquired using a Thermo Fisher Nicolet iS50 spectrometer. The elemental compositions of the catalysts were determined by inductively coupled plasma optical emission spectroscopy (ICP-OES, PerkinElmer 8300). Approximately 5 mg of each sample was dissolved in aqua regia in a Teflon-lined vessel and heated at 120 °C for 4 h to ensure complete dissolution. After cooling, the solution was diluted to 50 mL with deionized water. The resulting solution was further diluted by a factor of 20 prior to ICP-OES analysis. All measurements were performed in triplicate, and the average values were used to calculate the weight percentages of Cu and Co. The Brunauer–Emmett–Teller (BET) surface area of the nanoparticles was measured with an ASAP 2460 instrument at 77 K. Prior to measurement, the samples were degassed under vacuum at 150 °C for 12 h. For the isotope-labelling experiments, liquid products were analysed by ^1H nuclear magnetic resonance (NMR) spectroscopy using a Bruker 400 MHz spectrometer.

Electrochemical tests were performed using an Autolab PGSTAT128N potentiostat/galvanostat in a standard three-electrode system. An Ag/AgCl electrode (CHI111, CH Instruments) and a platinum electrode were used as the reference and counter electrodes, respectively. The working electrode was the as-prepared catalyst loaded on copper foam (geometric area: 1 cm^2; loading: 1.47 mg cm^{-2}). Nitrate reduction experiments were conducted in an H-type cell separated by a Nafion 117 membrane. The electrolyte (0.2 M K_2SO_4 with varying KNO_3 concentrations) was purged with argon for 30 min prior to each experiment. Chronoamperometry measurements were performed at different potentials to quantify the reaction products. All potentials reported *vs.* Ag/AgCl were converted to the reversible hydrogen electrode (RHE) scale using the formula: $E(vs.\ \text{RHE}) = E(vs.\ \text{Ag/AgCl}) + 0.059 \times \text{pH} + 0.205$ V. For long-term stability tests, electrolysis was conducted at a constant potential for 105 h. For comparison, flow-cell tests were conducted using a custom-built flow cell, and the catholyte (50 mM KNO_3 in 0.2 M K_2SO_4) was circulated at 1 mL min^{-1} using a peristaltic pump.

In situ FTIR measurements were performed in a customized thin-layer electrochemical cell using a Thermo Nicolet iS50 spectrometer equipped with a liquid nitrogen-cooled MCT detector. A catalyst-coated glassy carbon disk was used as the working electrode. The electrolyte (0.2 M K_2SO_4 + 50 mM KNO_3) was purged with Ar for 30 min. Spectra were recorded at different applied potentials with a resolution of 4 cm^{-1}.

Product analysis

The concentration of produced NH_3 in the catholyte was quantified by the indophenol blue method. Briefly, a diluted sample (2 mL) was mixed with 2.0 mL of an alkaline solution containing 5.0 wt% salicylic acid and 5.0 wt% sodium citrate. Subsequently, 1 mL of 0.05 M NaClO and 0.20 mL of 1.0 wt% sodium nitroprusside solution were added. After incubation in the dark at room temperature for 2 h, the absorbance at 655 nm was measured using a microplate reader. The concentration of NO_2^- was determined by the *N*-(1-naphthyl)ethylenediamine dihydrochloride colorimetric method, with the absorbance measured at 540 nm using a microplate reader.

The NH_3 yield rate and faradaic efficiency (FE) were calculated using the following equations:

$$\text{Yield } (\mu g\ h^{-1}\ cm^{-2}) = (C \times V)/(t \times S)$$

$$\text{FE } (\%) = (n \times F \times C \times V \times 10^{-6})/(M \times Q) \times 100\%$$

where C is the concentration of total ammonia quantified by the indophenol blue method and expressed as NH_3 equivalent ($\mu g\ mL^{-1}$), V is the electrolyte volume (mL), t is the electrolysis time (h), S is the geometric area of the electrode (cm^2), $n = 8$ is the number of electrons transferred for the NO_3^- to NH_3 conversion, F is Faraday's constant (96 485 C mol^{-1}), $M = 17$ g mol^{-1} is the molar mass of NH_3, and Q is the total charge passed (C). The factor 10^{-6} converts μg to g for unit consistency.[44]

Energy-related metrics including nitrate conversion, energy efficiency, and specific energy consumption were calculated according to standard electrochemical equations, and the detailed calculation procedures are provided in the SI.

Density functional theory (DFT) simulation

The projector augmented wave (PAW) method was employed to accurately describe the many-body interactions between ionic

cores and valence electrons. Within the generalized gradient approximation (GGA) framework, the revised Perdew–Burke–Ernzerhof (RPBE) functional was adopted to model the exchange–correlation potential. A plane-wave basis set with a cutoff energy of 520 eV was used. For Brillouin-zone integration, a 3 × 3 × 1 Monkhorst–Pack *k*-point mesh was applied, and electronic smearing was treated with the first-order Methfessel–Paxton scheme using a width of 0.1 eV. The convergence criteria were set as follows: energy change $\leq 1 \times 10^{-5}$ eV and atomic forces ≤ 0.02 eV $Å^{-1}$. The van der Waals interactions were accounted for using the Grimme-D3 method with zero damping. For model construction, a slab model of the (111) facet was built based on monoclinic CuO, with a 15 Å vacuum layer introduced along the surface normal direction to avoid interactions between periodic slabs; similarly, a (111) facet slab model was constructed using cubic Co_3O_4, also with a 15 Å vacuum layer introduced on both sides to eliminate interference. Implicit solvation effects were considered in all calculations, and no additional potential (U = 0 V) was applied for the computation of the free-energy diagram of the eNRA.

Results and discussion

Hollow Co_3O_4/CuO nanoparticles were synthesized *via* a template-free hydrothermal method followed by thermal annealing in air at 400 °C. The Co/Cu molar ratios were precisely tuned to 2 : 1, 1 : 1, and 1 : 2 by adjusting the initial precursor concentrations (denoted as H-Co2Cu1, H-Co1Cu1, and H-Co1Cu2, respectively). SEM images reveal that H-Co2Cu1 nanoparticles exhibit a uniform, quasi-spherical morphology with an average diameter of approximately 500 nm (Fig. 2a). TEM further confirms a well-defined hollow structure with a shell thickness of ~30 nm (Fig. 2b). While H-Co1Cu1 and H-Co1Cu2 also maintain hollow structures, an increase in the Cu content leads to a decrease in the internal void size and a corresponding increase in shell thickness (Fig. S1). To further evaluate the hollow structure, solid CoCu nanoparticles (denoted as S-CoCu) were synthesized for comparison (Fig. S2). Nitrogen adsorption–desorption measurements reveal a clear hysteresis loop, indicating the presence of mesoporous pores. The BET surface area of H-Co2Cu1 (30.3 m^2 g^{-1}) is higher than that of S-CoCu (4.5 m^2 g^{-1}, Fig. S3), suggesting a more developed porous structure. XRD analysis was used to identify the crystalline phases of the synthesized materials. As shown in Fig. 2c, H-Co2Cu1 exhibits characteristic diffraction peaks that can be indexed to cubic Co_3O_4 (JCPDS no. 78-1969) and monoclinic CuO (JCPDS no. 48-1548). Similarly, all Co_3O_4/CuO composites with different Co/Cu molar ratios exhibit diffraction features corresponding to both oxide phases.[45] Tuning the Co/Cu ratio from 2 : 1 to 1 : 2 led to a decrease in the relative intensity of the Co_3O_4 peak at 36.8°, and an increase in intensities of the CuO peaks at 35.4° and 38.7° (Fig. S4). This compositional trend is further confirmed by the ICP-OES results (Table S1).

XPS was conducted to explore the surface chemical states of the Co_3O_4/CuO hollow spheres. The Cu 2p spectrum (Fig. S5a) shows two main peaks at 933.9 and 953.5 eV, corresponding to Cu $2p_{3/2}$ and Cu $2p_{1/2}$, respectively, confirming the presence of Cu^{2+} species in CuO.[46] The Co 2p spectrum (Fig. S5b) shows two main peaks at 779.7 and 794.6 eV, which can be assigned to Co $2p_{3/2}$ and Co $2p_{1/2}$ and are indicative of mixed Co^{2+}/Co^{3+} oxidation states characteristic of a spinel Co_3O_4 structure. HRTEM reveals nanosized domains in close contact exhibiting distinct lattice fringes corresponding to these different phases (Fig. 2d). Lattice spacings of 0.239 nm and 0.253 nm are consistent with the (311) plane of Co_3O_4 and the (002) plane of CuO, respectively. Furthermore, EDS elemental mapping (Fig. 2e) demonstrates the uniform distribution of Cu, Co, and O throughout the entire hollow structure. It should be noted that the uniform elemental distribution reflects the intimate integration of the nanosized grains of CuO and Co_3O_4 within the shell, suggesting the presence of abundant interfaces while maintaining their individual crystalline phases.

The eNRA performance of the Co_3O_4/CuO catalysts was evaluated in 0.2 M K_2SO_4 electrolyte containing different concentrations of KNO_3 at room temperature.[47] Linear sweep voltammetry (LSV) was first conducted to assess electrocatalytic behaviour. As shown in Fig. 3a, the onset potential for nitrate reduction is about −0.4 V, and the current density increases monotonically as the potential becomes more negative. Compared with the electrolyte without nitrate, the presence of NO_3^- significantly increases the cathodic current density of H-Co2Cu1, which also confirms its activity towards nitrate reduction. The NH_3 selectivity was then quantified over a wide nitrate concentration window (Fig. 3b–e). The

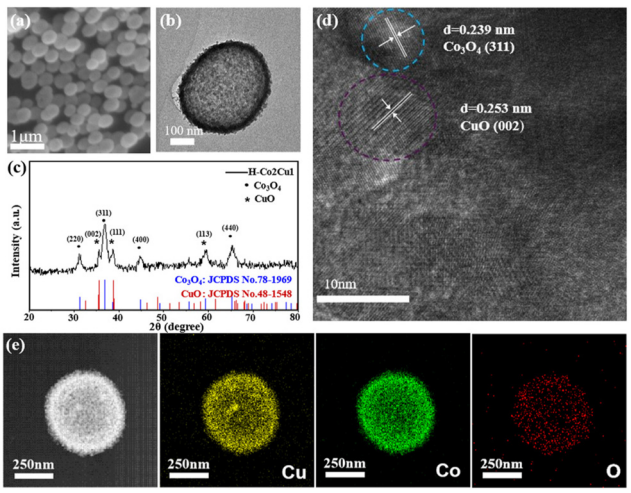

Fig. 2 (a) SEM and (b) TEM images of the uniform H-Co2Cu1 nanoparticles with a hollow structure. (c) XRD pattern confirming the coexistence of Co_3O_4 and CuO phases within H-Co2Cu1. (d) HRTEM image of a H-Co2Cu1 nanoparticle. (e) HRTEM image of a single H-Co2Cu1 nanoparticle with corresponding EDS elemental mapping of Cu, Co, and O.

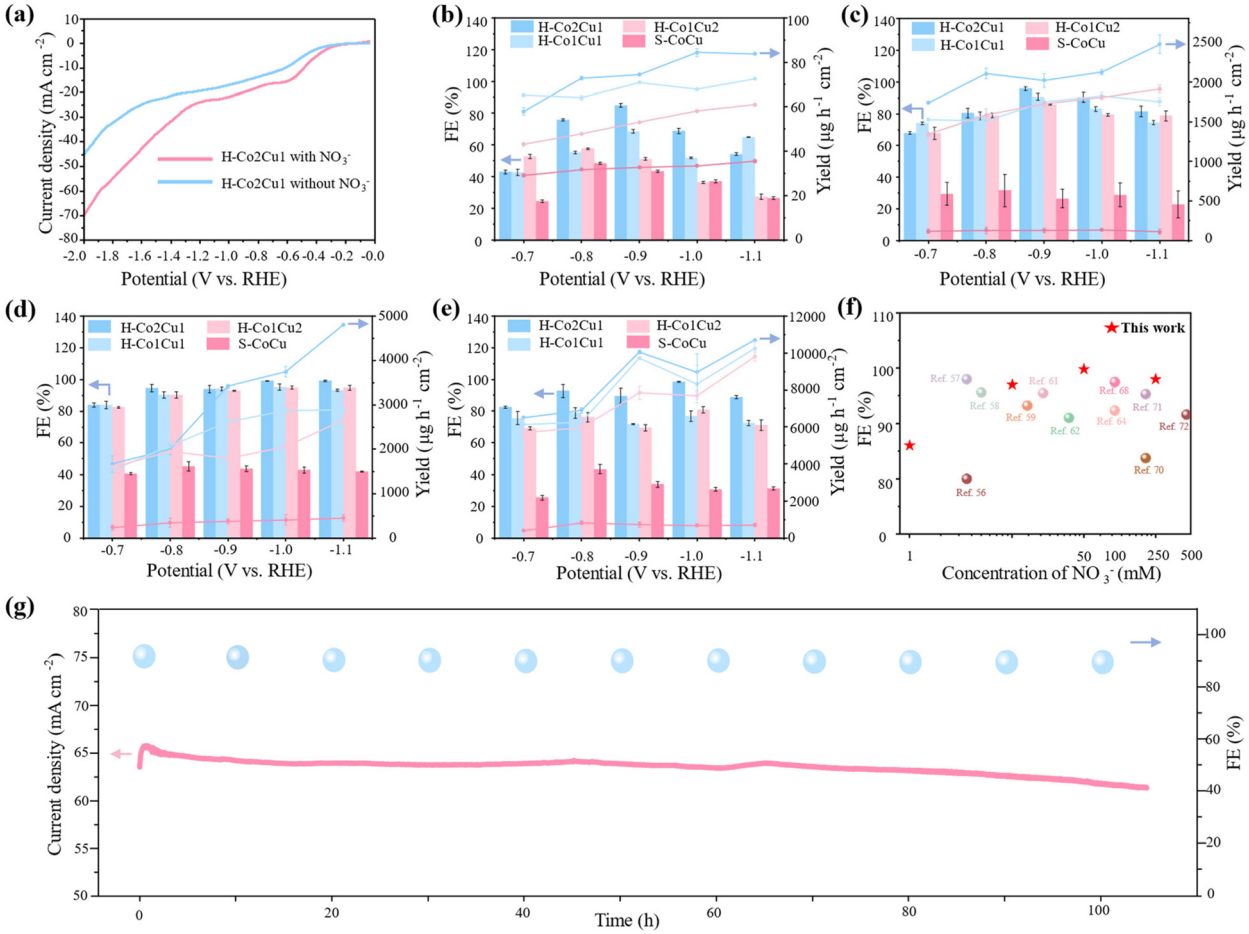

Fig. 3 eNRA performance of the H-Co2Cu1, H-Co1Cu1, H-Co1Cu2 catalysts and S-CoCu nanoparticles measured in an H-type electrolyzer. (a) LSV curves of H-Co2Cu1 in 0.2 M K_2SO_4 electrolyte with and without 10 mM NO_3^-. (b–e) Faradaic efficiency (FE) for NH_3 and NH_3 yield rate at (b) 1 mM, (c) 10 mM, (d) 50 mM, and (e) 250 mM KNO_3 in 0.2 M K_2SO_4 electrolyte for the four catalysts (bars denote NH_3 FE, and lines denote NH_3 yield rate). (f) Comparison of the electrocatalytic NRA performance of H-Co2Cu1 with that of recently reported electrocatalysts. (g) Chronoamperometric response and corresponding NH_3 FE for H-Co2Cu1 recorded at −1.0 V in 0.2 M K_2SO_4 with 50 mM KNO_3 electrolyte during consecutive recycling tests.

NH_3 FE reaches a maximum at −0.9 V (86–99%) across the tested nitrate concentrations and declines at −1.0 V due to the onset of hydrogen evolution. The hollow Co_3O_4/CuO catalysts exhibit higher NH_3 FEs than S-CoCu across the whole tested nitrate concentration range, with enhancements of approximately 2–3 times. This performance gap highlights the benefit of the hollow architecture for eNRA. Among the hollow series, H-Co2Cu1 exhibits the best overall performance across all concentration regimes compared with H-Co1Cu1 and H-Co1Cu2. Specifically, at a low nitrate concentration of 1 mM KNO_3, the NH_3 FE reaches a maximum of 86.7% at −0.9 V, with a corresponding NH_3 yield rate of 74 μg h^{-1} cm^{-2} (Fig. 3b). At 10 mM KNO_3, the FE peaked at 97.3% at the same potential (Fig. 3c). With increasing nitrate concentration, the performance remained outstanding. At 50 mM and 250 mM KNO_3, the FE achieves remarkable values of 99.8% and 98.7% at −1.0 V, respectively (Fig. 3d and e). To further clarify the trade-off among activity, selectivity, and energy efficiency, additional experiments were carried out over a wider potential range (−0.6 to −1.3 V) using H-Co2Cu1 at a representative nitrate concentration of 50 mM (Fig. S6). As the potential becomes more negative, both the total and NH_3 partial current densities increase continuously, while the NH_3 faradaic efficiency first increases and then slightly declines at more negative potentials. Meanwhile, the energy efficiency reaches a maximum of 43.99% at −0.8 V and gradually decreases at higher overpotentials, indicating that −0.8 to −1.0 V provides a balanced operating window with high NH_3 partial current density, high FE, and reasonably high energy efficiency, with a minimum energy consumption of 26.95 kWh kg^{-1} NH_3 (Table S2).[22,48–55] In addition, analysis of the liquid products at 50 mM NO_3^- shows that the selectivity toward the intermediate NO_2^- remains below 2% across the tested potentials (Fig. S7), indicating negligible intermediate accumulation. Meanwhile, H-Co2Cu1 achieves efficient nitrate removal with

over 95% NO_3^- conversion within 1 h at an initial concentration of 50 mM (Fig. S8). As summarized in Fig. 3f and Table S3, H-Co2Cu1 delivers a superior ammonia formation rate and maintains an FE comparable to or higher than state-of-the-art catalysts across the 1–250 mM concentration window in neutral solution.[56–72] These results demonstrate the broad concentration adaptability of this catalyst and its practical potential for treating nitrate-contaminated waters of variable compositions.

Control experiments confirmed that the detected NH_3 originated specifically from nitrate reduction, as negligible ammonia was produced in the absence of NO_3^- (Fig. S9). To further verify the nitrogen source of the produced ammonia, isotopic labeling experiments were conducted using $K^{15}NO_3$ as the sole nitrate source under the operating conditions of −1.0 V, and 50 mM nitrate. The resulting ^1H NMR spectra clearly show the characteristic doublet of $^{15}NH_4^+$, confirming that ammonia is exclusively derived from nitrate reduction (Fig. S10). Moreover, to exclude the contribution from the copper foam support, control experiments were performed using bare copper foam, which exhibited markedly inferior performance (Fig. S11). This result confirms that the outstanding electrochemical activity originates from the hollow heterostructured Co_3O_4/CuO catalyst rather than the substrate. Importantly, a durability test of H-Co2Cu1 at −1.0 V for 105 h (Fig. 3g) shows a stable current density of approximately 65 mA cm^{-2} and a consistently high NH_3 FE of about 99%, with no observable morphological changes after long-term operation (Fig. S12). To evaluate the practical applicability of the catalyst, H-Co2Cu1 was tested in a flow cell with identical catalyst loading (1.47 mg cm^{-2}) and electrode area (1 cm^2). Compared with the H-cell configuration, the total current density increased by 3.4 times, leading to a 3-fold enhancement in the NH_3 yield, while maintaining an NH_3 FE of 79% at −1.0 V (Fig. S13). These results collectively demonstrate the robust long-term operational stability and practical applicability of the hollow heterostructured catalyst for eNRA.

The capability of the hollow Co_3O_4/CuO catalyst to maintain high ammonia selectivity over a broad nitrate concentration range suggests efficient formation and consumption of reaction intermediates under both dilute and concentrated conditions. To gain insight into the underlying mechanisms responsible for this behaviour, we separately examined the roles of the hollow architecture and the ensemble effect at the Co_3O_4/CuO interface during eNRA. The effect of the hollow structure on intermediate formation and consumption was investigated using *in situ* FTIR spectroscopy to directly monitor nitrogen-containing species under reaction conditions. For H-Co2Cu1 (Fig. 4a), no obvious signals related to key reaction intermediates were observed at the open-circuit potential (OCP). Upon applying increasingly cathodic potentials, a negative absorption band at approximately 1331 cm^{-1} emerges, which can be attributed to the asymmetric N–O stretching vibration of adsorbed NO_3^-.[73–75] Meanwhile, a band emerging at approximately 1110 cm^{-1} corresponds to the deoxygenated intermediate *NO, indicating the onset of nitrate reduction on the catalyst surface.[73,76–78] At more negative potentials, additional vibrational features appear in the high-wavenumber region. Bands at ~3730 cm^{-1} and ~3625 cm^{-1} are associated with –NH–related species, while the band at ~1431 cm^{-1} corresponds to NH_3/NH_4^+, collectively evidencing the formation of reduced nitrogen products.[76,79,80] Notably, distinct bands at ~1168 cm^{-1} and ~1650 cm^{-1}, characteristic of adsorbed $*NH_2OH$, are clearly observed, suggesting the presence of partially hydrogenated nitrogen intermediates during the reaction.[76,81] In contrast, S-CoCu exhibits substantially weaker infrared signals for these nitrogen-containing intermediates under identical conditions (Fig. 4b). The suppressed intermediate signatures are consistent with the lower nitrate reduction activity and ammonia selectivity observed, indicating less effective intermediate formation and conversion on the solid catalyst surface.

To explore the role of the Co_3O_4/CuO interface, hollow CuO nanoparticles were prepared and evaluated as a reference catalyst (Fig. S14). At both dilute (1 mM) and concentrated (250 mM) nitrate concentrations, the hollow CuO catalyst shows a lower NH_3 FE than the Co_3O_4/CuO catalysts at optimal potentials (Fig. S15). To gain mechanistic insight into this difference, DFT simulations were performed to explore the free-energy profiles of eNRA on Co_3O_4/CuO and CuO.[80,82–84] A Co-doped CuO model was constructed to represent the ensemble effect of CuO domains adjacent to the Co_3O_4 domains in Co_3O_4/CuO catalysts (denoted as Co–CuO), thereby capturing the local electronic perturbation in the interfacial vicinity while avoiding uncertainties associated with explicitly modeling interfaces between crystallographically distinct oxides. Prior studies suggested that the eNRA process is a multistep proton-coupled electron transfer pathway.[85] Accordingly, we calculated the free-energy changes for each elementary step along the reaction sequence: $*NO_3 \rightarrow *NO_2 \rightarrow *NO \rightarrow *NHO \rightarrow *NH_2O \rightarrow *NH_2OH \rightarrow *NH_2 \rightarrow *NH_3$ (Fig. 5a and Fig. S16, S17). In the NO_3^- adsorption step, Co incorporation can decrease the adsorption energy of NO_3^-. To quantify this difference, charge density difference analyses were performed for both models (Fig. 5b and c). For Co–CuO, the electron gain of NO_3^- is $0.63e^-$, which is higher than that on the pure CuO

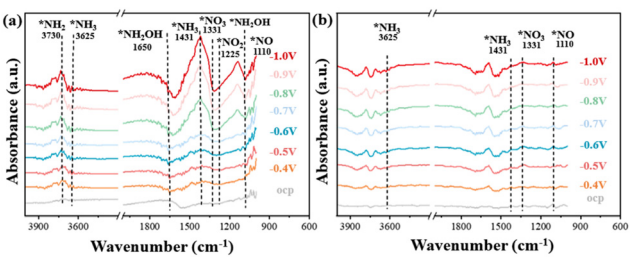

Fig. 4 Mechanistic investigation of NO_3^- electroreduction. *In situ* attenuated total reflection Fourier transform infrared (ATR-FTIR) spectra for (a) H-Co2Cu1 and (b) S-CoCu nanoparticles in a solution of 50 mM KNO_3 and 0.2 M K_2SO_4 under different applied potentials.

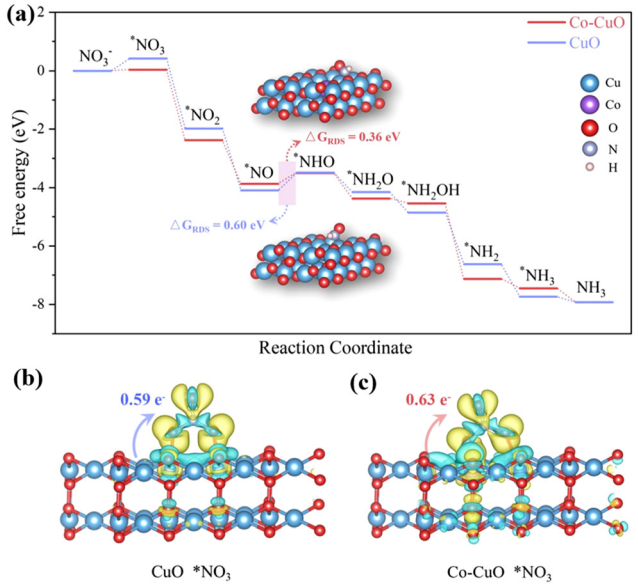

Fig. 5 DFT simulations of eNRA: (a) calculated free-energy diagrams and corresponding structural models for the reaction pathways of CuO and Co–CuO. Differential charge density maps for NO_3* adsorption on (b) CuO and (c) Co–CuO (yellow and blue regions represent electron accumulation and depletion, respectively).

(0.59e^-). This enhanced charge transfer indicates stronger adsorption, which facilitates NO_3^- activation.[83] In addition, the free-energy diagram shows that the rate-determining step (RDS) of the reaction is the hydrogenation of *NO to *NHO. In the presence of Co, the site exhibits a reduced uphill barrier for the RDS (0.36 eV) compared with pure CuO (0.60 eV). As a further reference, eNRA energetics were evaluated on a Co_3O_4 surface (Fig. S18), where the same RDS is observed but with a significantly higher uphill free-energy change (0.75 eV). Together, these results indicate that the ensemble effect at the Co_3O_4/CuO interface more effectively lowers the energetic requirement of the potential-determining step than either single-phase CuO or Co_3O_4 alone.

Conclusion

In summary, we have developed a hollow heterostructured Co_3O_4/CuO catalyst that achieves highly selective and stable eNRA under neutral conditions across a broad nitrate concentration range. The catalyst shows an NH_3 FE exceeding 97% from 10 to 250 mM, and maintains 86% even in highly dilute (1 mM) solutions. The enhanced performance can be attributed to the combined effects of the hollow architecture and the ensemble effect at the Co_3O_4/CuO interface. The hollow structure promotes nitrate utilization within the catalyst interior, while the intimate integration of Co_3O_4 and CuO facilitates efficient conversion of nitrate intermediates. This structural engineering strategy to tune the catalysts provides an approach for efficient electrochemical conversion and remediation processes involving dilute feeds, holding particular promise for adaptive wastewater treatment and sustainable nitrogen-recovery technologies.

Author contributions

Li Yao, Shao Ye, and Zhe Li contributed equally to this work. Li Yao performed materials synthesis, characterization and electrocatalytic analysis. Shao Ye performed DFT calculations. Bo Shen supervised the research. All authors participated in discussions and provided suggestions. Bo Shen and Wenlei Zhu contributed to the writing.

Conflicts of interest

The authors declare no conflict of interest.

Data availability

The data supporting the findings of this study are available within the article and its supplementary information (SI). Supplementary information is available. See DOI: https://doi.org/10.1039/d6gc00484a.

Additional data related to the electrochemical measurements and computational models are available from the corresponding author upon reasonable request.

Acknowledgements

This work was financially supported by the National Key R&D Program of China (2025YFA1511200), and the Natural Science Foundation of Guangdong Province (2026A1515010021). W. Z. would like to acknowledge support from the State Key Laboratory of Water Pollution Control and Green Resource Recycling, and the State Key Laboratory of Analytical Chemistry for Life Science (SKLACLS2503).

References

1 H. Zhang, H. Wang, X. Cao, M. Chen, Y. Liu, Y. Zhou, M. Huang, L. Xia, Y. Wang, T. Li, D. Zheng, Y. Luo, S. Sun, X. Zhao and X. Sun, *Adv. Mater.*, 2024, **36**, 2312746.
2 Z. Zhao, X. Zhang, Y. Li, S. Qin and X. Liu, *Green Chem.*, 2026, **28**, 2935–2947.
3 Z. Li, C. Yang, B. Xu, L. Yao, W. Zhu and Y. Cui, *Energy Mater.*, 2024, **4**, 400046.
4 M. Zheng, Y. Wan, Z.-H. Huang, F. Kang and R. Lv, *Adv. Mater.*, 2026, **38**, e14834.
5 F. Edition, *WHO Chron.*, 2011, **38**, 104–108.
6 Y. Wang, Y. Zeng, J. Xie, C. Wang, C. Zhou, L. Song, K. Ma and H. Yue, *Green Chem.*, 2025, **27**, 1763–1770.
7 R. Jia, Y. Wang, C. Wang, Y. Ling, Y. Yu and B. Zhang, *ACS Catal.*, 2020, **10**, 3533–3540.

8 R. Li, H. Li, Y. Liu, J. Luo, Q. Sui, K. Wang, J. Xia and Y. Jiang, *Green Chem.*, 2025, **27**, 11107–11114.
9 F. Zhao, J. Xin, M. Yuan, L. Wang and X. Wang, *Water Res.*, 2022, **209**, 117889.
10 Z. Li, J. Luo, L. Yao, Y. Gan, Z. Wang, H. Zheng, M. Cai, C. Ding, X. Luo and Y. Cui, *Chin. Chem. Lett.*, 2025, 112141.
11 G. Zhou, Z. Xiong, X. Lian and Y. Ding, *J. Water Process Eng.*, 2024, **60**, 105130.
12 A. Fumasoli, E. Morgenroth and K. M. Udert, *Water Res.*, 2015, **83**, 161–170.
13 Y. Shahaf, T. K. Slot, S. Avidan, J. E. Dick and D. Eisenberg, *ACS Catal.*, 2025, **15**, 7254–7262.
14 J. Bai, Z. Dong, X. Jiang, Q. Zhou, J. Zhao, J. Mei, Z. Tan, T. Liao and Z. Sun, *Adv. Sci.*, 2025, **12**, e08614.
15 S. Yin and Y. Wang, *Molecules*, 2025, **30**, 3910.
16 G. Wen, J. Liang, L. Zhang, T. Li, Q. Liu, X. An, X. Shi, Y. Liu, S. Gao and A. M. Asiri, *J. Colloid Interface Sci.*, 2022, **606**, 1055–1063.
17 H. Jiang, G. F. Chen, O. Savateev, J. Xue, L. X. Ding, Z. Liang, M. Antonietti and H. Wang, *Angew. Chem.*, 2023, **135**, e202218717.
18 Y. Han, J. Shang, S. Yin, R. Cao, J. Zhang, W. Jiang and G. Liu, *Green Chem.*, 2024, **26**, 8145–8160.
19 G. Jiang, Z. Liu, S. He, Y. Liu, X. Tang, X. Lv, F. Dong and H. Liu, *ACS ES&T Eng.*, 2024, **4**, 2912–2922.
20 J. Ma, W. Wei, G. Qin, T. Xiao, W. Tang, S. Zhao, L. Jiang and S. Liu, *Water Res.*, 2022, **208**, 117862.
21 Z. Mo, W. Guo, L. Xu, Y. Chen, S. Zhou and B. Liu, *Green Chem.*, 2025, **27**, 14478–14506.
22 M. Wang, W. Song, H. Zou, G. Liu and S. You, *Adv. Funct. Mater.*, 2026, e28731.
23 M. Yang, W. Wang, Z. Zhao, S. Yue, K. Liu, P. Wang and S. Zhan, *Adv. Funct. Mater.*, 2026, e30516.
24 W. Zhang, F. Guo, W. Gong, D. Yang, X. Yin, F. Jia, W. Wei, Y. Yao and L. Zhang, *Angew. Chem., Int. Ed.*, 2026, **65**, e16226.
25 H. Jiang, G.-F. Chen, O. Savateev, J. Xue, L.-X. Ding, Z. Liang, M. Antonietti and H. Wang, *Angew. Chem., Int. Ed.*, 2023, **62**, e202218717.
26 J. Li, G. Zhan, J. Yang, F. Quan, C. Mao, Y. Liu, B. Wang, F. Lei, L. Li, A. W. M. Chan, L. Xu, Y. Shi, Y. Du, W. Hao, P. K. Wong, J. Wang, S. X. Dou, L. Zhang and J. C. Yu, *J. Am. Chem. Soc.*, 2020, **142**, 7036–7046.
27 D. Liu, L. Qiao, S. Peng, H. Bai, C. Liu, W. F. Ip, K. H. Lo, H. Liu, K. W. Ng and S. Wang, *Adv. Funct. Mater.*, 2023, **33**, 2303480.
28 J. Liang, Z. Li, L. Zhang, X. He, Y. Luo, D. Zheng, Y. Wang, T. Li, H. Yan, B. Ying, S. Sun, Q. Liu, M. S. Hamdy, B. Tang and X. Sun, *Chem*, 2023, **9**, 1768–1827.
29 W. Gao, K. Xie, J. Xie, X. Wang, H. Zhang, S. Chen, H. Wang, Z. Li and C. Li, *Adv. Mater.*, 2023, **35**, 2202952.
30 P. Li, Y. Liu, L. Xie, G. Wang, X. Lu, J. Li, X. Wu, Y. Jiang and W. Zhu, *Angew. Chem., Int. Ed.*, 2025, **64**, e202504499.
31 Z. Li, L. Wang, Y. Cai, J.-R. Zhang and W. Zhu, *J. Hazard. Mater.*, 2022, **440**, 129828.
32 W. Mei, C. W. Chang, Z. Li, X. Wang, Y. Qie, Q. Liu, R. C. Davis, Z. Wu, Y. Yue and C. Yang, *Adv. Mater.*, 2025, **37**, 2507363.
33 F.-Y. Chen, Z.-Y. Wu, S. Gupta, D. J. Rivera, S. V. Lambeets, S. Pecaut, J. Y. T. Kim, P. Zhu, Y. Z. Finfrock and D. M. Meira, *Nat. Nanotechnol.*, 2022, **17**, 759–767.
34 T. Zhao, Y. Chen, K. Wang and S. H. Ho, *Environ. Sci. Technol.*, 2026, **60**, 7605–7627.
35 S. Liang, X. Teng, H. Xu, L. Chen and J. Shi, *Angew. Chem., Int. Ed.*, 2024, **63**, e202400206.
36 G. Liao, R. L. Smith Jr, H. Guo and X. Qi, *Green Chem.*, 2024, **26**, 11797–11831.
37 B. Shen, L. Huang, J. Shen, X. Hu, P. Zhong, C. Y. Zheng, C. Wolverton and C. A. Mirkin, *ACS Nano*, 2023, **17**, 4642–4649.
38 Y. Cai, R. Yang, J. Fu, Z. Li, L. Xie, K. Li, Y.-C. Chang, S. Ding, Z. Lyu, J.-R. Zhang, J.-J. Zhu, Y. Lin and W. Zhu, *Nat. Synth.*, 2024, **3**, 891–902.
39 Q. Gao, B. Yao, H. S. Pillai, W. Zang, X. Han, Y. Liu, S.-W. Yu, Z. Yan, B. Min, S. Zhang, H. Zhou, L. Ma, H. Xin, Q. He and H. Zhu, *Nat. Synth.*, 2023, **2**, 624–634.
40 X. Jin, L. Sun, X. Wang, R. Wang, L. Yan, A. C. Fisher, J.-M. Lee and X. Wang, *Angew. Chem., Int. Ed.*, 2026, **65**, e24566.
41 Y. Zeng, C. Priest, G. Wang and G. Wu, *Small Methods*, 2020, **4**, 2000672.
42 J. Ni, J. Yan, F. Li, H. Qi, Q. Xu, C. Su, L. Sun, H. Sun, J. Ding and B. Liu, *Adv. Energy Mater.*, 2024, **14**, 2400065.
43 L. Gu, N. Song, Z. Wu, H. Luo, J. Chen and J. Yang, *Angew. Chem., Int. Ed.*, 2025, **65**, e25547.
44 X. Gu, J. Zhang, S. Guo, Y. Zhang, L. Xu, R. Jin and G. Li, *J. Am. Chem. Soc.*, 2025, **147**, 22785–22795.
45 J. Zhang, H. Lu, T. Yao, X. Ji, Q. Zhang, L. Meng, J. Feng and H. Wang, *Chin. Chem. Lett.*, 2024, **35**, 108450.
46 Z. Wang, Y. Zhang, H. Xiong, C. Qin, W. Zhao and X. Liu, *Sci. Rep.*, 2018, **8**, 6530.
47 K. Zhang, P. Sun, Y. Huang, M. Tang, X. Zou, Z. Pan, X. Huo, J. Wu, C. Lin and Z. Sun, *Adv. Funct. Mater.*, 2024, **34**, 2405179.
48 Y. Li, Y. Liu, M. Zhang, L. Li, Z. Jiang, B. Han, B. Wang and J. Li, *Angew. Chem., Int. Ed.*, 2025, **64**, e202417631.
49 Y. Li, L. Li, S. Xu, K. Cui, T. Wang, Z. Jiang and J. Li, *Angew. Chem., Int. Ed.*, 2024, **63**, e202407810.
50 T. G. Eshetu, M. E. Ayalew, A. A. Mitiku, Q.-N. Ha, M. Z. Silitonga, V.-N. Tran and D.-H. Kuo, *Chem. Eng. J.*, 2026, **527**, 171695.
51 Q. Li, Y. Li, B. Xu, J. Yang and Y. Wang, *Angew. Chem., Int. Ed.*, 2025, **64**, e202510139.
52 X. Ouyang, W. Qiao, Y. Yang, B. Xi, Y. Yu, Y. Wu, J. Fang, P. Li and S. Xiong, *Angew. Chem., Int. Ed.*, 2025, **64**, e202422585.
53 Y. Feng, X. Lv, H. Wang, L. Wang, M.-L. Sun, J.-T. Ren and Z.-Y. Yuan, *Adv. Energy Mater.*, 2025, **15**, e03022.
54 S. Zhang, Q. Song, X. Cui, G. Guo, J. Li, X. Liu and M. Li, *Appl. Catal., B*, 2026, **385**, 126297.

55 X. Xu, Y. Ge, C. Fu, R. Wang, C. Liu, Z. Yin, Q. Zhou and W. Yang, *J. Colloid Interface Sci.*, 2026, **706**, 139749.
56 L. Fang, Y. Wang, S. Lu, Y. Zhang, Y. Li, F. Yin and H. Liu, *Appl. Catal., B*, 2025, **381**, 125816.
57 Q. Song, W. Dong, J. Wang, S. Zhang, M. Li, J. Chen, S. Zhang and J. Lu, *Chem. Eng. J.*, 2025, **520**, 165364.
58 X. Fan, C. Lai, L. Qin, M. Zhang, H. Yan, S. Liu, D. Ma, Q. Liu and L. Tang, *Chem. Eng. J.*, 2025, **522**, 168046.
59 X. Liu, Y. Wang, Z. Hu, B. Yang, R. L. Smith Jr, Y. Su and X. Qi, *Appl. Catal., B*, 2025, **371**, 125254.
60 C. Wang, Z. Liu, L. Dong, F. Du, J. Li, C. Chen, R. Ma, C. Li and C. Guo, *J. Power Sources*, 2023, **556**, 232523.
61 B. Liu, H. Liu, S. Qiang, J. Dai, J. Yan, J. Yu, Y. T. Liu and B. Ding, *Adv. Funct. Mater.*, 2026, e29295.
62 K. Li, B. An, J. Zhu, X. Yu, B. Wang, S. Sun, F. Li, Y. Tang, Z. Li and K. Zhao, *Chem. Eng. J.*, 2025, **520**, 166141.
63 J. Wei, Y. Liu, Z. Wu, L. Han, A. Deng, Q. Li, C. Jiang, J. Liu, L. Gan and Y. Zhang, *Adv. Funct. Mater.*, 2025, **35**, e13566.
64 J. Zhong, H. Duan, M. Cai, Y. Zhu, Z. Wang, X. Li, Z. Zhang, W. Qu, K. Zhang and D. Han, *Angew. Chem., Int. Ed.*, 2025, **64**, e202507956.
65 Y. Li, J. Wei, H. Lin, Y. Guo, X. Lu, S. Liu, H. Liu, M. Tang, J. Zhou and Y.-y. Li, *ACS Catal.*, 2025, **15**, 1672–1683.
66 H. Sun, W. Zhang, Y. Qi, Q. Xu, J. Han, R. Zhao, Y. Liu, J.-S. Qin and H. Rao, *ACS Catal.*, 2025, **15**, 18712–18722.
67 Q. Tian, X. Ye, L. Jing, W. Wang, Z. Zheng, A. Li, K. Xie, X. Huang, Q. Hu and H. Yang, *Angew. Chem.*, 2025, **137**, e202516919.
68 Y. Wang, T. Bao, L. Chen, C. Zhang, J. Wang, Y. Zou, Y. Xi, Z. Li, C. Yu and C. Liu, *Angew. Chem., Int. Ed.*, 2025, **64**, e202509090.
69 P. Liu, J. Yan, H. Huang and W. Song, *Chem. Eng. J.*, 2023, **466**, 143134.
70 N. Mukherjee, A. Adalder, S. Paul, N. Barman, R. Thapa, K. Mitra, R. Urkude and U. K. Ghorai, *Adv. Funct. Mater.*, 2025, **36**, e19797.
71 J. Wei, H. Lin, Y. Li, Y. Guo, S. Liu, M. Sun and Y.-y. Li, *J. Hazard. Mater.*, 2025, **493**, 138264.
72 A. Yan, Y. Feng, X. Zhang, J. Sun, J. Wei, C. Shi, L. Xia, S. Wang, H. Zhang and Y. Guo, *Small*, 2025, **21**, e06256.
73 L. Wu, J. Feng, L. Zhang, S. Jia, X. Song, Q. Zhu, X. Kang, X. Xing, X. Sun and B. Han, *Angew. Chem., Int. Ed.*, 2023, **62**, e202307952.
74 N. Zhou, Z. Wang, N. Zhang, D. Bao, H. Zhong and X. Zhang, *ACS Catal.*, 2023, **13**, 7529–7537.
75 M. Zuo, Y. Kong, H. Zhou, Y. Chen, Y. Sun, S. Li and L. Han, *Adv. Funct. Mater.*, 2026, **36**, e13364.
76 Z. Chen, Y. Zhao, H. Huang, G. Liu, H. Zhang, Y. Yan, H. Li, L. Liu, M. Liu, D. Wang and J. Zeng, *J. Am. Chem. Soc.*, 2025, **147**, 18737–18746.
77 X. Sun, Y. He, M. Wang, Q. Cheng, Y. Huan, S. Liu, J. Liu, T. Qian, C. Yan and J. Lu, *ACS Nano*, 2025, **19**, 8189–8199.
78 W. Chen, W. Zeng, Z. Chen, Y. Zou, C. Zhang, S. Ye, J. Ding, X. Han and W. Hu, *Angew. Chem., Int. Ed.*, 2025, **65**, e202516997.
79 J. Zhou, M. Wen, R. Huang, Q. Wu, Y. Luo, Y. Tian, G. Wei and Y. Fu, *Energy Environ. Sci.*, 2023, **16**, 2611–2620.
80 J.-Y. Fang, Q.-Z. Zheng, Y.-Y. Lou, K.-M. Zhao, S.-N. Hu, G. Li, O. Akdim, X.-Y. Huang and S.-G. Sun, *Nat. Commun.*, 2022, **13**, 7899.
81 S.-N. Zhang, P. Gao, Q.-Y. Liu, Z. Zhang, B.-L. Leng, J.-S. Chen and X.-H. Li, *Nat. Commun.*, 2024, **15**, 10877.
82 Z. Chen, G. Liu, Y. Zhao, Y. Yan, Q. Ke, C. Wan, Z. Zhang, J. Yuan, H. Li, M. Liu and J. Zeng, *Angew. Chem., Int. Ed.*, 2025, **65**, e23740.
83 Z. Ye, B. Shen, D. Kang, J. Shen, J. Huang, Z. Wang, L. Huang, C. M. Wolverton and C. A. Mirkin, *Nat. Synth.*, 2024, **3**, 922–929.
84 X. Zhong, Z. Wang, Y. He, M. Liu, F. Yang, M. Xu, H. Li, L. Cao, C. Yu, Y. Zhang, Y. Wang, H. Wang, Y. Zhu, W. Shi and M. Liu, *ACS Nano*, 2026, **20**, 3110–3122.
85 S. Chen, Z. Zhu, K. Song, H. Zhang, D. Luo, T. Cao, Y. Zou, C. Liu, L. Gan, D. Zhang, Y. Han and J. Huang, *J. Am. Chem. Soc.*, 2025, **147**, 36494–36507.